ACS APPLIED MATERIALS & INTERFACES

Research Article

www.acsami.org

Synthesis of Nitrogen- and Sulfur-Codoped 3D Cubic-Ordered Mesoporous Carbon with Superior Performance in Supercapacitors

Deyi Zhang,*[,†,‡,§] Liweng Zheng,[§] Ying Ma,[†] Longyan Lei,[§] Qinglin Li,[†] Yan Li,[‡] Heming Luo,[§] Huixia Feng,[§] and Yuan Hao[†]

[†]State Key Laboratory of Gansu Advanced Non-ferrous Metal Materials, Lanzhou University of Technology, Lanzhou 730050, China

[‡]Key Laboratory of Eco-Environment-Related Polymer Materials of the Ministry of Education, Northwest Normal University, Lanzhou 730070, China

[§]College of Petrochemical Technology, Lanzhou University of Technology, Lanzhou 730050, China

Supporting Information

ABSTRACT: In this contribution, nitrogen- and sulfur-codoped 3D cubic-ordered mesoporous carbon (KNOMC) materials with controlled dopant content (10.0−4.6 atom % for nitrogen and 0.94−0.75 atom % for sulfur) are presented, using KIT-6 as the template and pyrrole as the precursor, and its supercapacitive behavior is also investigated. The presented materials exhibit excellent supercapacitive performance by combining electrical double-layer capacitance and pseudocapacitance as well as the enhanced wettability and improved conductivity generated from the incorporation of nitrogen and sulfur into the framework of carbon materials. The specific capacitance of the presented materials reaches 320 F g^{-1} at a current density of 1 A g^{-1}, which is significantly larger than that of the pristine-ordered mesoporous carbon reported in the literature and can even compete with some metal oxides and conducting polymers.

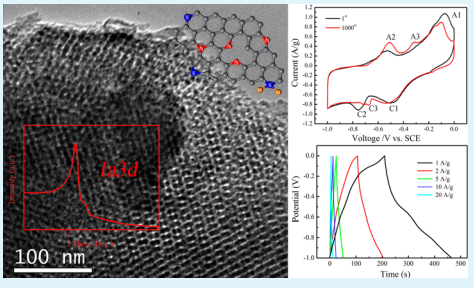

KEYWORDS: *nitrogen and sulfur codoping, cubic-ordered mesoporous carbon, supercapacitors*

INTRODUCTION

In recent years, the quick development of hybrid electric vehicles and portable electronic devices promoted by increasingly serious air pollution due to the enormous consumption of fossil fuel accelerated the growing need for high-power energy resources. Currently, in comparison with batteries and conventional capacitors, supercapacitors have the advantages of high power density, fast charge/discharge processes, and long cycle life and have been considered a good choice for high-power energy to meet the need for fast growth in power required by devices.[1−3]

In principle, the capacitive behavior of supercapacitors can be categorized into two types according to the mechanism of electrical energy storage:[1] (1) electrical double-layer capacitance (EDLC), which stores charges at the interface between the electrode and electrolyte;[4−7] (2) pseudocapacitance generated by reversible redox or faradaic charge-transfer reactions,[8] such as transition-metal oxides[9,10] and conducting polymers.[11] Generally, supercapacitors using carbon materials as an electrode mainly stored electrical energy in the form of EDLC. However, the energy stored in the supercapacitors based on EDLC is far lower than that of batteries, which limits their use in applications that require high power density.[4] The development of high-energy-density supercapacitors without sacrificing cycle life and high power density has thus been a key challenge for researchers. Carbon-based composites, such as λ-MnO_2/carbon,[12] Mn_2O_3/carbon,[13] polyaniline/graphene,[14] and polyaniline/ordered mesoporous carbon composites,[15] combining EDLC and pseudocapacitance have been explored to further improve the power and energy densities of the supercapacitors. Although these composites have exhibited enhanced capacitance and good cyclability, the trivial fabrication process, poor chemical stability in an acid medium, and unsatisfied compatibility with organic electrolytes limit their applications as high-power supercapacitor electrodes. Alternatively, chemical doping with heteroatoms, such as nitrogen, sulfur, boron, or phosphorus, can considerably improve the capacitance of carbon materials because of additional contributions from pseudocapacitance and enhanced electronic conductivity.[16−20] For example, nitrogen-doped graphene shows a remarkable performance as an electrode material of supercapacitors with a high specific capacitance of 280 F g^{-1}, which is about 4 times larger than that of pristine graphene.[21] Ma and co-workers reported that the specific capacitance of the nitrogen-doped hollow graphitic carbon spheres reaches 306 F g^{-1} at a current density of 0.1 A g^{-1} in 2 M H_2SO_4,[22] while Kim and coresearchers observed that the specific capacitance of the nitrogen-doped mesoporous carbons prepared by ammoxidation is enhanced by about 53% over that of pristine-ordered mesoporous carbon.[19] Very recently, the

Received: November 15, 2013
Accepted: January 28, 2014
Published: January 28, 2014

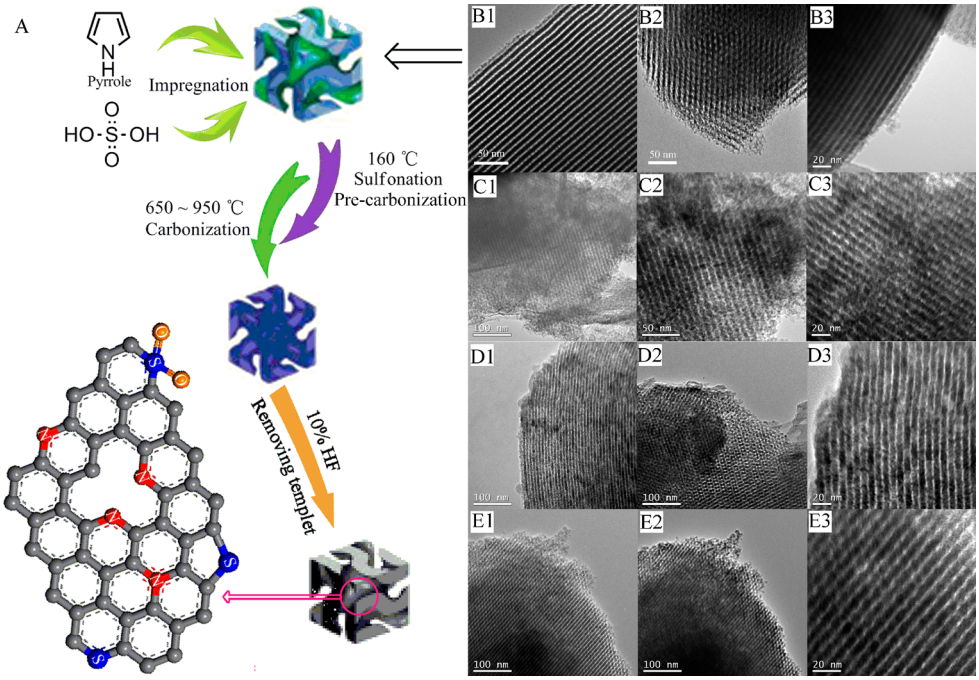

Figure 1. Scheme for the synthesis of KNOMC (A) and TEM images of KIT-6 (B1, B2, and B3), KNOMC-650 (C1, C2, and C3), KNOMC-800 (D1, D2, and D3), and KNOMC-950 (E1, E2, and E3), viewed along various directions.

enhanced supercapacitive behavior of sulfur-doped carbon materials due to the pseudocapacitive behavior related with oxidized sulfur species (sulfone and sulfoxides) was reported.[23−25] Zhao et al. reported that the specific capacitance of sulfur-doped mesoporous carbon derived from 4,40-thioldiphenol was improved by 72% over that of conventional ordered mesoporous carbon; the capacitance measured in an alkaline electrolyte was found to be proportional to the sulfur content.[23] Seredych and Bandosz also reported that the volumetric capacitance of sulfur-doped micro/mesoporous carbon−graphene composites reached 65 F cm^{-3}, which is higher than that of pristine-ordered mesoporous carbon;[24] meanwhile, the visible-light exposure and electrolyte oxygen content exhibited remarkable effection for the supercapacitive behavior of sulfur-doped carbon materials because of the photoactivity and oxygen reduction performance of these materials.[26]

Although the additional contribution from pseudocapacitance is believed to be the origination of the enhanced capacitance performance of the heteroatom-doped carbon materials, direct evidence (reversible redox peaks originating from the faradaic reaction) of this presumption is so far absent. In this work, nitrogen- and sulfur-codoped 3D cubic-ordered mesoporous carbons (KNOMCs) were synthesized using KIT-6 as the template and pyrrole as the precursor, and its capacitive performance as electrode materials of supercapacitors is also investigated. The reported materials exhibited a high specific capacitance of 320 F g^{-1} at a current density of 1 A g^{-1} in 2 M potassium hydroxide (KOH). The supplementary pseudocapacitance and enhanced wettability as well as the improved conductivity generated from the incorporation of nitrogen and sulfur into the carbon framework are believed to be responsible for the excellent capacitance performance of KNOMC materials. The pseudocapacitance originating from the redox or faradaic charge-transfer reaction because of the chemical doping of heteroatoms into the frameworks of carbon materials was proven by the apparent reversible redox peaks shown on the cyclic voltammetry (CV) curves.

EXPERIMENTAL DETAILS

Synthesis of the KIT-6 Template. Bicontinuous cubic (*Ia*3*d*) mesoporous silica KIT-6 was obtained following the method reported by Kleitz et al.[27] Briefly, 2.0 g of Pluronic P123 (EO20PO70EO20, MW = 5800, Aldrich) was added to the mixed solution of 72 g of distilled water and 4 g of 35% HCl. After complete dissolution, 2.0 g of butanol was added and stirred at 35 °C for 1 h. Then 4.3 g of tetraethyl orthosilicate (Aldrich, 99.9%) was added to the homogeneous clear solution. The mixture was left under stirring for 24 h at 35 °C and subsequently heated for 24 h at 100 °C in a Teflon-lined autoclave vessel. The solid product obtained was filtered and dried at 100 °C, and then the template was removed by extraction in an ethanol−HCl mixture. The KIT-6 template was then obtained after calcination at 550 °C under atmosphere.

Synthesis of KNOMC Materials. A nanocasting strategy was adopted to synthesize the KNOMC materials using KIT-6 as the template. The general synthesis process is summarized and illustrated in Figure 1A. First, pyrrole monomers polymerize to form an oligomer catalyzed by sulfuric acid in the pores of the KIT-6 template, and then the oligomer reacts with sulfuric acid to generate a sulfonated product of the oligomer via electrophilic substitution at 160 °C. Finally, the KNOMC materials were obtained through further carbonization and removal of the template. In brief, 1.0 mL of pyrrole (Aldrich, 99%) was mixed with 0.5 mL of absolute alcohol, and then a transparent light-yellow solution was obtained when 0.1 mL of sulfuric acid (98%) was added immediately. The solution was slowly dropped onto the surface of 1.0 g of the KIT-6 template. The impregnated sample was heated at 80 °C for 2 h under vacuum to evaporate alcohol and then precarbonized for 8 h at 160 °C. The impregnation/precarbonization process was repeated. Then, the resultant brown product was carbonized under an argon atmosphere at 350 °C for 2 h and was completely carbonized at 650−950 °C for 2 h. Finally, the silica template was removed by dissolution in a HF (10 wt %) aqueous solution to obtain the KNOMC materials. The KNOMC series materials synthesized at different carbonization temperatures are referred to as KNOMC-*x*, where *x* denotes the carbonization temperature.

dx.doi.org/10.1021/am405128j | ACS Appl. Mater. Interfaces 2014, 6, 2657−2665

Characterization. Transmission electron microscopy (TEM) experiments were conducted on a JEM-2010 microscope operated at 200 kV. X-ray photoelectron spectroscopy (XPS) was performed on a Thermo Multilab 2000, using monochrome Al Kα as the excitation source. The small-angle X-ray scattering (SAXS) patterns were collected on a X'Pert X-ray defractometer (Phillips) using Cu Kα radiation. The d spacing values were calculated by the formula $d = \lambda/2 \sin\theta$, and the unit cell parameters were calculated from the formula $a = 6^{1/2}d_{211}$.[28] The wall thickness was calculated from $W_T = a/3.0919 - D/2$, where a represents the unit cell parameter and D is the pore diameter calculated from the nitrogen sorption measurements.[29] Nitrogen adsorption/desorption isotherms were performed at 77 K on a Micromeritics ASAP 2020 volumetric adsorption analyzer. The pore-size distribution was calculated by employing the Barrett–Joyner–Halenda (BJH) method from the adsorption branch, and the pore volume was estimated from the amount of nitrogen gas adsorbed at a relative pressure P/P_0 of 0.995. The specific surface area (S_{BET}) was determined by utilizing the Brunauer–Emmett–Teller (BET) equation.

Electrochemical Measurements. Electrical measurements were carried out at room temperature on an electrochemical analyzer, CHI 910B (Shanghai, Chenhua Limited Co.), using a KOH (2 M) aqueous solution as the electrolyte. A three-electrode system using KNOMC as the working electrode, a platinum slice as the counter electrode, and a saturated calomel electrode (SCE) as the reference electrode was employed to evaluate the supercapacitive behavior of the presented materials. To prepare the working electrode, KNOMC samples were ground with acetylene black (10 wt %) and poly(tetrafluoroethylene) (5 wt %) and then pressed onto nickel foam that served as a current collector.

RESULTS AND DISCUSSION

The representative TEM images of the KIT-6 template and the KNOMC materials synthesized at different carbonization temperatures are shown in parts B, C, D, and E of Figure 1, respectively. The TEM images of the KNOMC materials clearly exhibit well-ordered mesoporous structure; linear arrays of mesopores are arranged in regular intervals. Synthesized KNOMCs with body-centered-cubic *Ia*3*d* structure types are reversed replicas of the KIT-6 mesoporous silica template, as shown in Figure 1D2; the cross-sectional TEM images of the KNOMC samples clearly display the same well-ordered 3D body-centered-cubic mesostructure as that of the KIT-6 template.

The ordered arrangement of the carbon nanorods in KNOMC materials is further substantiated by the well-resolved SAXS peak. As shown in Figure 2, the SAXS patterns for all materials exhibit three well-resolved diffraction peaks, associated with the 211, 220, and 332 reflections of 3D cubic *Ia*3*d* space groups, respectively.[27,28,30] The nearly the same SAXS patterns of KNOMC materials and the KIT-6 template indicate that the aforementioned KNOMC materials are faithful inverse replicas of this template. The unit cell parameters for the KIT-6 template and KNOMC materials evaluated from the SAXS data are summarized in Table 1. As shown in Table 1, framework shrinkage during the pyrogenation/carbonization process of the precursor can be observed; the cell parameter (a) was calculated to be 9.2, 8.7, and 7.8 nm for KNOMC-650, KNOMC-800, and KNOMC-950, respectively. The shift of the diffraction peaks to higher angle provides direct evidence for this shrinkage phenomenon.[31] Meanwhile, framework shrinkage is observed to be more serious at higher temperatures, as demonstrated by the decrease of the cell parameter and wall thickness with increasing carbonization temperature. More serious decomposition of the C–N and C–S bonds at higher temperatures may be responsible for this phenomenon.

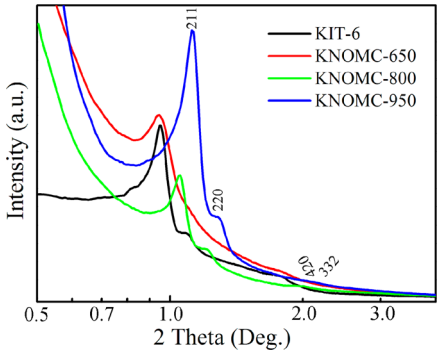

Figure 2. SAXS patterns of the KIT-6 template and KNOMC materials.

The nitrogen adsorption/desorption isotherms and pore-size distribution of KNOMC materials and the KIT-6 template are shown in Figure 3, respectively. The textural parameters of the corresponding samples are listed in Table 1. As shown in Figure 3A, the isotherms of KNOMC materials exhibit the same type IV adsorption behavior; meanwhile, a H1-type hysteresis loop is present at the higher relative pressure of 0.4–0.9 in the adsorption isotherms, which indicated the mesoporous nature of the synthesized codoped carbon materials.[32,33] The sharp increase of the adsorption amount at the initial step of the hysteresis loop corresponding to the capillary condensation of nitrogen inside the ultralarge mesopores reveals the narrow pore-size distribution of the codoped materials.[34] The isotherms of all samples of KNOMC materials exhibit two major capillary condensation steps from the uniform-sized structural and complementary mesopores, respectively. The complementary mesopores may be generated from the combination of mesopores due to the collapse of the pore wall. The step of the adsorption branch of KNOMC-800 and KNOMC-950 shifts to lower relative pressure compared with that of the KIT-6 template, implying a decrease of the pore size. From Figure 3B, it can be observed that the pore-size distribution centers on 2.72, 2.98, and 3.68 nm for KNOMC-650, KNOMC-800, and KNOMC-950, respectively, while the KIT-6 template has a wall thickness of 3.5 nm, which suggests that a large portion of the pores originates from the pore wall of the silica template, agreeing well with the TEM results. Meanwhile, the pore-size distribution curves of the KNOMC materials show another pronounced shoulder peak at about 12 nm, which originates from the combination of mesopores due to the collapse of the pore wall. These shoulder peaks gradually disappear with increasing carbonization temperature, which is probably due to the fact that higher carbonization temperatures result in decomposition of the C–N and C–S bonds and a corresponding decrease of the nitrogen and sulfur content, which reduces the structural defect caused by the incorporation of nitrogen and sulfur atoms in the carbon framework. The average pore sizes (D_{AV}) calculated by the BJH model are 6.20, 3.27, and 4.29 nm for KNOMC-650, KNOMC-800, and KNOMC-950, respectively. The calculated BET surface areas are 1064, 693, and 880 $m^2\ g^{-1}$ for KNOMC-650, KNOMC-800, and KNOMC-950, respectively, while the single-point total pore volumes reach 1.78, 0.75, and 1.09 $cm^3\ g^{-1}$, respectively.

The chemical compositions of the synthesized KNOMC materials were analyzed using XPS. As shown in Table 2,

dx.doi.org/10.1021/am405128j | ACS Appl. Mater. Interfaces 2014, 6, 2657–2665

Table 1. Textural Parameters of the KNOMC Materials

sample ID	d_{100} [nm]	a [nm]	W_t [nm]	D [nm]	D_{av} [nm]	S_{BET} [m^2 g^{-1}]	V_T [cm^3 g^{-1}]	V_M [cm^3 g^{-1}]
KIT-6	9.2	22.5	3.5	7.60	6.15	944	1.32	1.26
KNOMC-650	9.2	22.6	5.9	2.72, 12.9	6.2	1064	1.78	1.68
KNOMC-800	8.9	21.8	5.6	2.98, 11.42	3.27	693	0.75	0.69
KNOMC-950	7.8	19.1	4.3	3.68,11.0	4.29	880	1.09	1.04

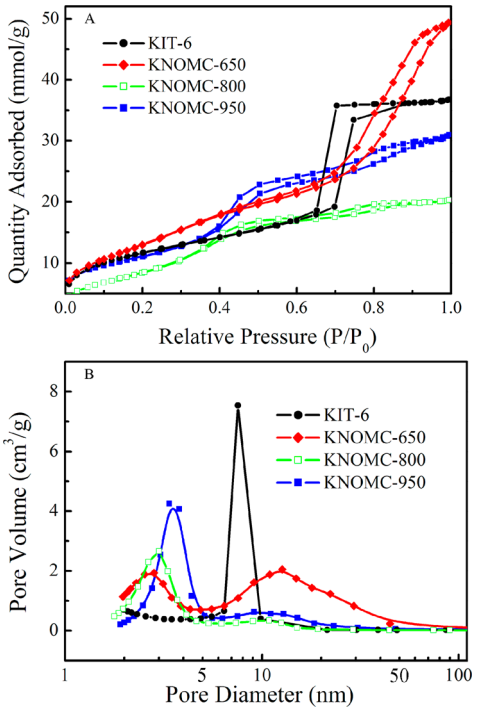

Figure 3. Nitrogen adsorption/desorption isotherms (A) and pore-size distributions (B) of the KIT-6 template and KNOMC materials.

reasonable amounts of both nitrogen and sulfur were detected in all samples. KNOMC-650 and KNOMC-800 exhibit their approximate nitrogen contents, but for KNOMC-950, it decreases to 4.6 atom %. These results indicate good thermal stability for KNOMC materials when the carbonization temperature is below 800 °C. However, when the temperature is higher than 800 °C, decomposition of the C−N bond becomes serious. For sulfur, a slight fluctuation of the sulfur content (from 0.75 to 0.94 atom %) was observed, which also demonstrates good thermal stability of the C−S bond in the framework of KNOMC materials. Besides variation of the sulfur species, the oxygen content increased from 3.13 to 5.96 atom % as the carbonization temperature increased from 650 to 950 °C.

The incorporation of nitrogen and sulfur heteroatoms within the carbon framework of KNOMC materials was confirmed by the XPS spectra (Figure 4). As shown in Figure 4, the XPS spectra of the N 1s orbital exhibit two peaks at 398.4 and 400.6 eV. One of the peaks around 398.4 eV is commonly attributed to the pyridinic-like nitrogen species, which is bound to two carbon atoms and donates one p electron to the aromatic π system, and another peak around 400.6 eV can be assigned to the quaternary nitrogen bound within a graphite-like framework, which is incorporated into the graphene layer and replaces a carbon atom within a graphene plane.[35−37] The XPS spectra of the S 2p orbital exhibit a higher complexity due to spin−orbit coupling phenomena, which show several peaks at 164.1, 165.3, and 168.2 eV for all samples. In spite of that, all of the peaks are referred to carbon-bound sulfur atoms: the peaks around 164.1 eV represent sulfur atoms bound in cyclic carbon structures in an aromatic environment, such as thiophenic-like sulfur,[38−40] and the peak around 165.3 eV can refer to the sulfoxide.[23,41] The peak around 168.2 eV is considered to be originated from −C−S(O_2)−C− sulphone bridges.[38,41] The XPS spectra of the C 1s orbital can be deconvolved as three peaks: the main deconvolved peak around 284.5 eV comes from aromatic or other sp^2-hybridized carbon atoms bound to neighboring carbon atoms or hydrogen,[35,42] while the slightly less pronounced deconvolved peaks at around 285.1 and 286.5 eV can be assigned to the electron-poor carbon bound to nitrogen or sulfur.[36,43−45] For O 1s, the XPS spectra can be deconvolved as three peaks corresponding to the binding energies (BEs) of C═O (530.8 eV), C−O (533.1 eV), and C−OH (534.2 eV) species, respectively.[23,46] Overall, the results of XPS characterization illuminated that the nitrogen and sulfur heteroatoms were firmly incorporated into the primarily aromatic carbon backbone.

The dopant species of the nitrogen and sulfur heteroatoms within the carbon framework of KNOMC materials were observed to be dependent on the carbonization temperature. As

Table 2. Summary of XPS Peak Analysis on the KNOMC Materials

	KNOMC-650			KNOMC-800			KNOMC-950		
sample	BE (eV)	rel intens (%)	content (atom %)	BE (eV)	rel intens (%)	content (atom %)	BE (eV)	rel intens (%)	content (atom %)
C 1s	284.5	31.8	86.41	284.5	35.1	84.53	284.5	21.7	88.62
	285.1	47.7		285.1	43.3		285.1	46.4	
	286.5	20.5		286.5	21.6		286.5	31.9	
N 1s	400.6	64.9	9.72	400.6	61.9	10.08	400.6	80.1	4.61
	398.4	35.1		398.4	38.1		398.4	19.9	
S 2p	164.1	35.7	0.75	164.1	39.3	0.94	164.1	32.8	0.81
	165.3	17.0		165.3	26.4		165.3	23.4	
	168.2	47.3		168.2	34.3		168.2	43.8	
O 1s	530.8	61.7	3.13	530.8	73.5	4.45	530.8	45.1	5.96
	533.1	19.1		533.2	12.4		533.2	9.1	
	534.2	19.2		534.2	14.1		534.2	45.9	

dx.doi.org/10.1021/am405128j | ACS Appl. Mater. Interfaces 2014, 6, 2657−2665

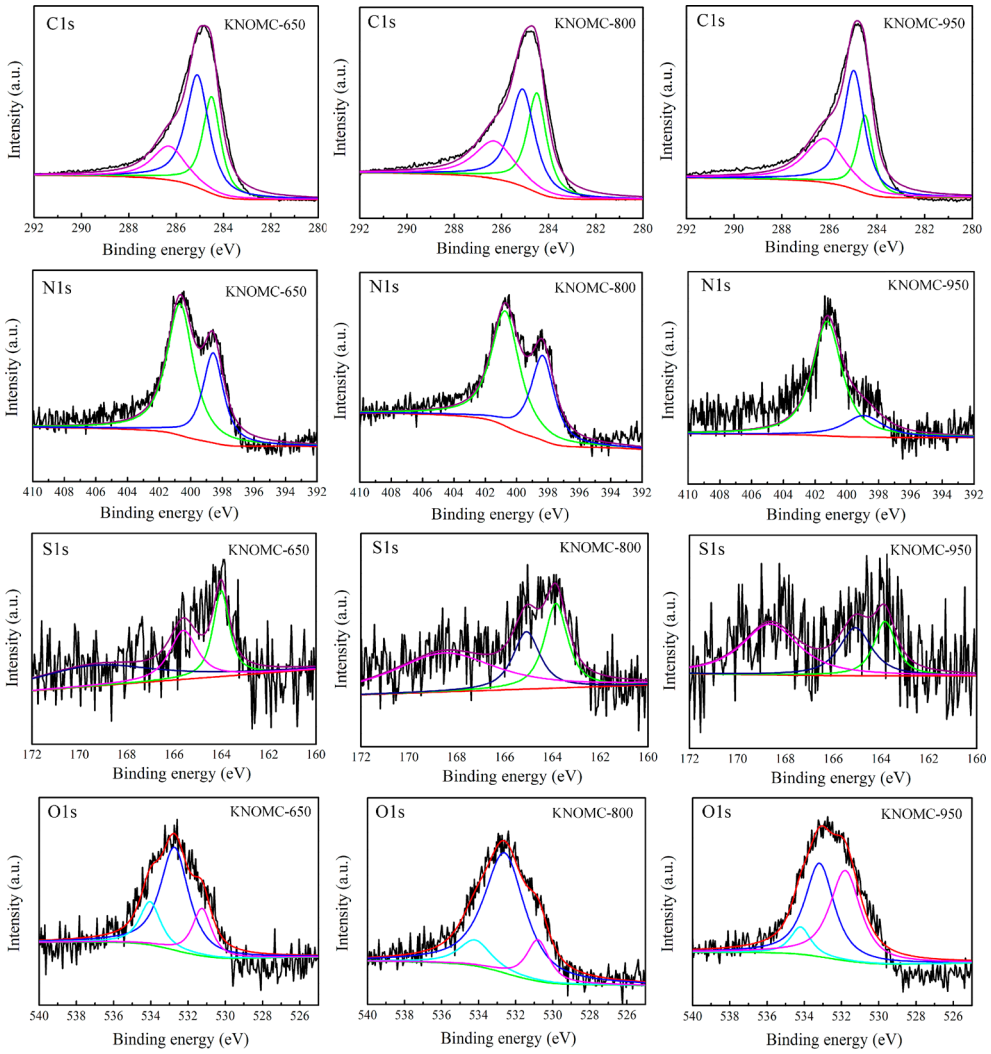

Figure 4. XPS spectra of C 1s, N 1s, S 2p, and O 1s for KNOMC materials.

shown in Table 2, the relative content of the graphite-like nitrogen species increases from 61.9 to 80.1% with increasing carbonization temperature, while the relative content of pyridinic-like nitrogen species correspondingly reduces from 38.1 to 19.9% (as shown in Figure 4 and Table 2). This may be due to the fact that graphite-like nitrogen species own higher BEs than pyridinic-like nitrogen species, and higher thermal stability is reasonably expected.

CV was used to evaluate the potential applications of KNOMC materials for supercapacitors. The CV curves of the fabricated electrodes at a scan rate of 1 mV s^{-1} are shown in Figure 5A. The CV curves of all electrodes show a rectangular-like CV shape overlapped by at least two pairs of approximate reversible redox peaks at ca. −0.1 and −0.5 V of the anodic scan and ca. −0.5 and −0.7 V of the cathodic scan. In an ideal EDLC, energy must be retrievable as discharge over the same potential range as that required to store the energy upon charging, which is reflected in rectangular-shaped cyclic voltammograms,[47] while pseudocapacitors are associated with fast and reversible oxidation/reduction (redox) or faradaic charge-transfer reactions, which is reflected in reversible redox peaks.[2,48] So, the synthesized KNOMC materials show a composite capacitance performance by combination with the EDLC and pseudocapacitance. It was reported that the pseudocapacitance of carbon materials originated from quinone−hydroquinone transitions;[26,49,50] however, in most cases, these transitions just displayed an unpronounced hump on the CV curves,[49,24] indicating a small contribution for the capacitance performance of carbon materials. In our experiment, because of the incorporation of nitrogen and sulfur heteroatoms within the framework of ordered mesoporous carbon, those redox peaks became strong and obvious and the contribution of the pseudocapacitance for the capacitance performance of KNOMC materials became well-pronounced correspondingly. Because of the high electronegativity of nitrogen atoms, the incorporation of nitrogen heteroatoms within the carbon framework, especially for the pyridinic-like nitrogen species, decreases the charge density of the aromatic carbon, which weakened the C═O and C−OH bonds and thus favored the quinone−hydroquinone transitions and generated pronounced pseudocapacitance. Meanwhile, the reversible redox related with oxidized sulfur species (sulfone and sulfoxides) also contributed to the pseudocapacitance of KNOMC materials.[23] The peak-to-peak separation (ΔE_p), which is the difference in the potential between the anodic and cathodic peaks, is associated with the rate of electron transfer.[51] Lower ΔE_p values correspond to a higher electron-transfer rate. It can be seen from Figure 5A that KNOMC-950 exhibits a

dx.doi.org/10.1021/am405128j | ACS Appl. Mater. Interfaces 2014, 6, 2657−2665

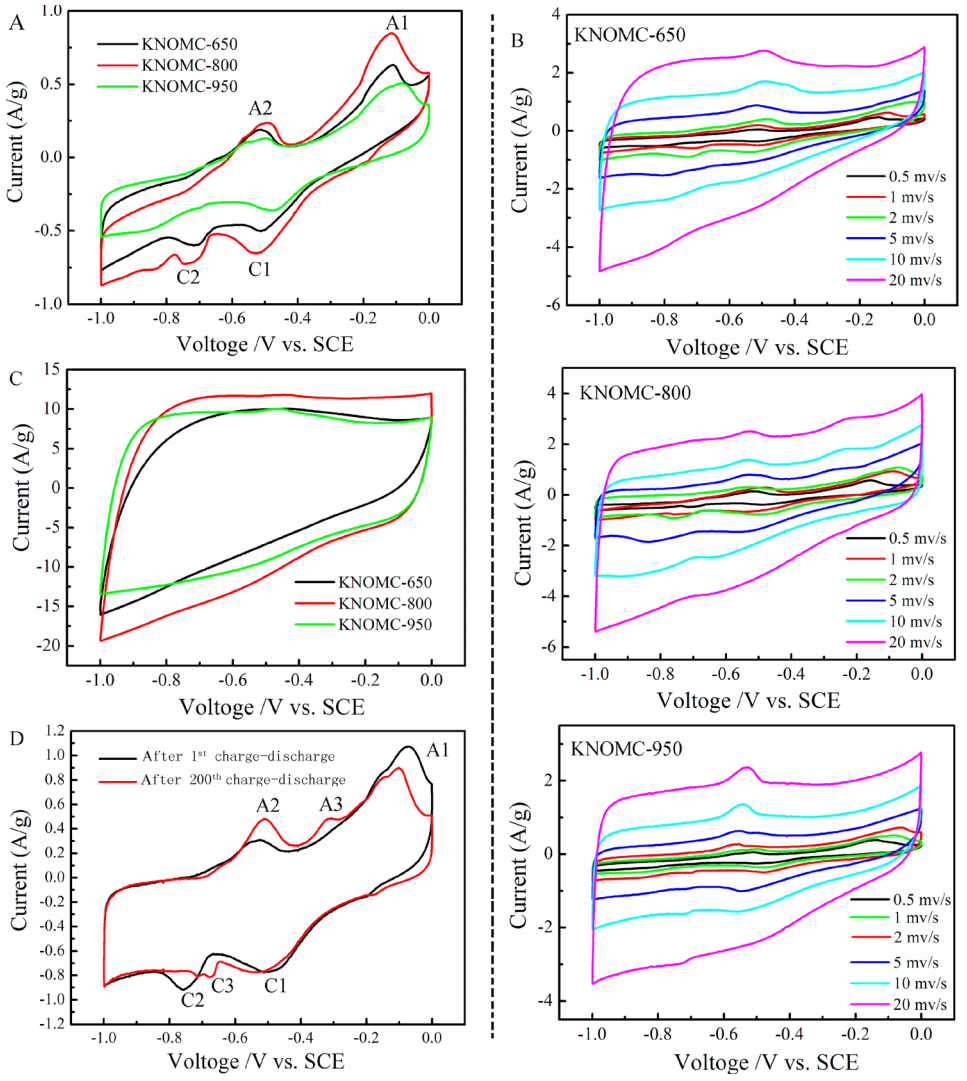

Figure 5. CV curves of the KNOMC electrodes at a scan rate of 1 mV s^{-1} (A). CV curves of the KNOMC electrodes at varying scan rate between 0.5 and 20 mV s^{-1} (B). CV curves of the KNOMC electrodes at a scan rate of 100 mV s^{-1} (C). CV curves of the KNOMC-850 electrodes at a scan rate of 1 mV s^{-1} after 1 and 200 cycles of charge/discharge (D).

lower ΔE_p value than KNOMC-650 and KNOMC-950, indicating faster electron-transfer rates. Figure 5B shows the CV curves of KNOMC materials at varying scan rate between 0.5 and 20 mV s^{-1}. It can be seen that for all materials two pairs of redox peaks can be clearly observed when the scan rate is lower than 2 mV s^{-1}; when the scan rate is higher than 2 mV s^{-1}, the first pairs of redox peaks at ca. −0.1 V of the anodic scan and ca. −0.5 V of the cathodic scan are diminished gradually. However, the second pairs of redox peaks at ca. −0.5 V of the anodic scan and ca. −0.7 V of the cathodic scan can still be clearly observed even at a scan rate of 20 mV s^{-1}. These results indicate that the second pairs of redox peaks have faster electron-transfer rates than the first pairs of redox peaks. As the scan rate increases to 100 mV s^{-1}, all redox peaks are diminished, but the CV curves for all samples still maintain an approximate rectangular-like shape with slight distortion, as shown in Figure 5C, illuminating a fast charge/discharge process and high power capability for KNOMC as electrode materials in a 2 M KOH aqueous solution. Figure 5D displays the CV curves of KNOMC-850 at a scan rate of 1 mV s^{-1} after 1 and 200 cycles of charge/discharge; it can be seen that after 200 cycles of charge/discharge the redox peaks still retain the same shape as that after the first charge/discharge, indicating the well reversibility of those redox peaks.

Figure 6A presents the charge/discharge curves of the KNOMC electrodes within a potential window of −1.0 to 0 V vs SCE at a current density of 1 A g^{-1}. During the charging, all KNOMC electrodes reveal an apparent voltage plateau around −0.1 V and another inconspicuous voltage plateau around −0.5 V, the voltage plateaus of which correspond to the two anodic peaks exhibited on the CV curves (Figure 5A). The plateaus of the discharging potential are observed at approximately −0.5 and −0.7 V, which are related to the cathodic peaks at ca. −0.5 and −0.7 V in the CV curves. These results illuminate that the supplementary pseudocapacitance originating from the redox or faradaic charge-transfer reactions contribute to the excellent capacitance performance of KNOMC materials. The specific capacitances calculated from the discharge curves reach 302 and 320 F g^{-1} at a current density of 1 A g^{-1} for KNOMC-650 and KNOMC-850, while that of KNOMC-950 is 185 F g^{-1}, the values of which are much larger than that of the pure ordered mesoporous carbon CMK-3 with a S_{BET} value of 1480 m^2 g^{-1} (129 F g^{-1} at 1 A g^{-1}), indicating that the incorporation of nitrogen and sulfur heteroatoms within the carbon framework

dx.doi.org/10.1021/am405128j | ACS Appl. Mater. Interfaces 2014, 6, 2657−2665

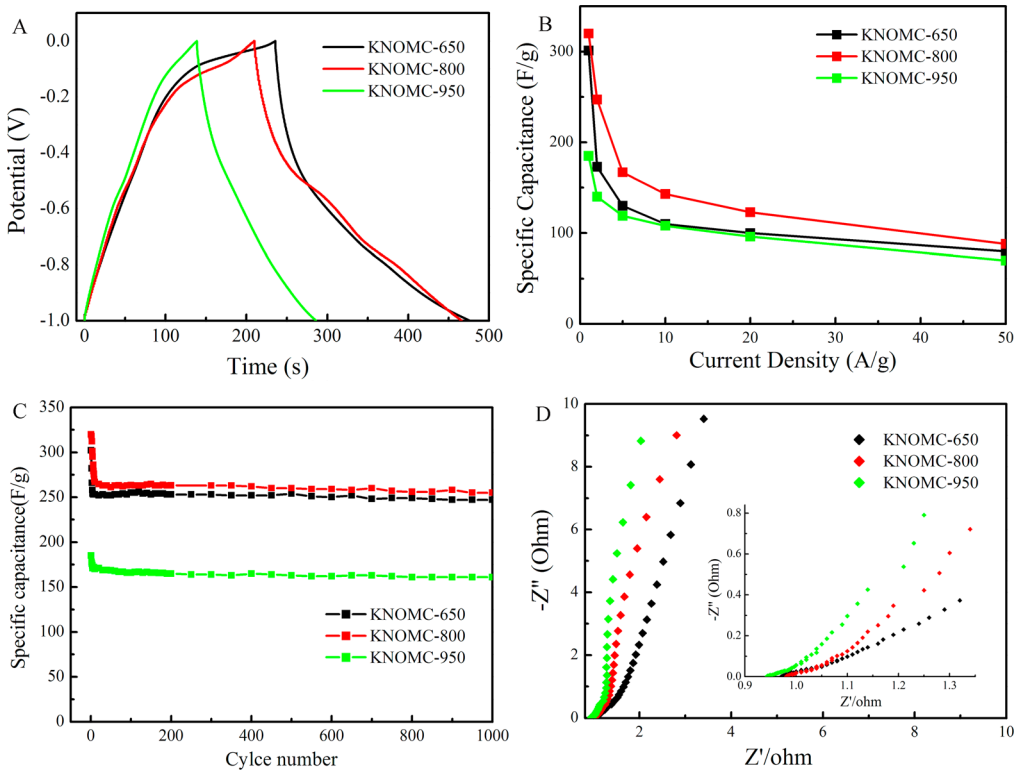

Figure 6. Galvanostatic charge/discharge curves of the KNOMC electrodes at a current density of 1 A g^{-1} (A). Specific capacitance of the KNOMC electrodes at different current densities (B). Cycle performance of the KNOMC electrodes at the current density of 1.0 A g^{-1} (C). Nyquist plots of the KNOMC electrodes (D).

effectively enhances the capacitance performance of ordered mesoporous carbon. A remarkable correspondence between the specific capacitance and the content of nitrogen and sulfur incorporated into the carbon framework proves credible evidence for this conclusion. Meanwhile, when the current density is larger than 2 A g^{-1}, the charge and discharge plateaus gradually disappear; all samples present a symmetrical triangle shape (as shown in Figure S1 in the Supporting Information), which is the typical characterization of the ideal electrical double-layer capacitor, indicating that the capacitance performance of the KNOMC electrodes mainly depends on the EDLC rather than the pseudocapacitance under the high current density. Moreover, even at a high current density of 10.0 A g^{-1}, there was no observation of obvious voltage drop at the current switches, indicating a quite low resistance of the KNOMC electrodes.[52] It was reported that the pyridinic-like nitrogen at the periphery of the graphene layers results in the attraction of ions, such as protons, and a consequent pseudocapacitive interaction.[53] For graphite-like nitrogen species, the nitrogen atom is inset into the carbon matrix and bonded to three carbon atoms, three valence electrons in the graphite-like nitrogen species form σ bonds, the fourth electron fills a p state, and the fifth electron forms a π^* state, giving the p-doping effect, which improves the conductivity of the carbon materials.[21] The sulfur dopant species, such as thiophenic-like sulfur and sulfone, may also play significant roles in modifying the surface properties, especially when a sulfur atom is bonded with benzene rings or shares a conjugated planar ring system with delocalized π-electron clouds instead of discrete alternating single or double bonds.[23] Meanwhile, the nitrogen and sulfur dopants modify the polarity of carbon matrixes because of the fact that carbon atoms adjacent to a nitrogen or sulfur atom possess a substantially high positive charge density to counterbalance the strong electronic affinity of the nitrogen and sulfur atoms,[23,54] which improves the wettability of the carbon matrix. This increased electrode/electrolyte wettability can promote ion diffusion in the interface between the electrode and electrolyte and the interior of KNOMC electrodes, thus improving the electrochemical performance.[55] So, the supplementary pseudocapacitance and enhanced wettability as well as the improved conductivity originating from the incorporation of nitrogen and sulfur into the carbon framework are responsible for the excellent capacitance performance of KNOMC materials.

Figure 6B shows the effect of the current density on the specific capacitance of the KNOMC electrodes. The values of the specific capacitance for the KNOMC electrodes are found to be strongly dependent on the current density. The sharp decrease of the specific capacitance when the current density is lower than 10 A g^{-1} may be caused by the gradual decrease of the pseudocapacitance with increasing current density due to the fast charge/discharge. Even so, the KNOMC electrodes still exhibit a relatively large value of specific capacitance at the relatively large current density, such as 109, 143, and 108 F g^{-1} for KNOMC-650, KNOMC-850, and KNOMC-950 at 10 A g^{-1}, respectively. The cycling stability of the KNOMC electrodes was examined using galvanostatic charge/discharge cycling at a current density of 1 A g^{-1} for 1000 cycles and is presented in Figure 6C. In the first 10 cycles, the specific capacitance decreases quickly, but the capacitance retention rate is approximately 100.0% during the 20−1000th cycles for all samples. After 1000 cycles, the specific capacitances are 247, 255, and 161 F g^{-1} for KNOMC-650, KNOMC-800, and KNOMC-950, respectively, the values of which reach 82%,

dx.doi.org/10.1021/am405128j | ACS Appl. Mater. Interfaces 2014, 6, 2657−2665

80%, and 87% of that of the first cycle, respectively, which demonstrates the good cycling performance of the KNOMC electrodes. Figure 6D shows the electrochemical impedance spectroscopy of the KNOMC electrodes in a 2 M KOH solution. The Nyquist plots of the KNOMC electrodes exhibit the typical features of porous electrodes with a 45° Warburg region at high-to-medium frequencies and an almost vertical line at low frequencies. At sufficiently high frequencies, the intercept at the real impedance (Z') axis is related to the internal resistance, including the resistance of the bulk electrolyte, the intrinsic resistance of the electrode materials, and their contact resistance with the nickel foam current collector. The internal resistance is found to be 0.97, 0.98, and 0.94 Ω for KNOMC-650, KNOMC-800, and KNOMC-950, respectively, which is lower than that of pure carbon CMK-3 (1.11 Ω), indicating that the incorporation of nitrogen and sulfur into the carbon framework can effectively enhance the conductivity of carbon materials.[56,57]

CONCLUSION

KNOMC synthesized via a nanocasting strategy using KIT-6 as the template and pyrrole as the precursor exhibits excellent capacitance performance. The specific capacitances reach 302, 320, and 185 F g^{-1} for KNOMC-650, KNOMC-850, and KNOMC-950, respectively, at a current density of 1 A g^{-1}, which is dependent on the content of nitrogen and sulfur incorporated into the carbon framework. At least two pairs of approximate reversible redox peaks originating from the redox or faradaic charge-transfer reactions are exhibited on the CV curves. The supplementary pseudocapacitance and enhanced wettability as well as the improved conductivity generated from the incorporation of nitrogen and sulfur into the carbon framework are believed to be responsible for the excellent capacitance performance of KNOMC materials.

ASSOCIATED CONTENT

Supporting Information

Galvanostatic charge/discharge curves of the KNOMC electrodes at different current densities. This material is available free of charge via the Internet at http://pubs.acs.org.

AUTHOR INFORMATION

Corresponding Author

*E-mail: lzdeyizhang@gmail.com.

Notes

The authors declare no competing financial interest.

ACKNOWLEDGMENTS

This work was supported by the National Natural Science Foundation of China under Grant 51063003, the Natural Science Foundation of Gansu under Grant 1112RJZA024, the State Key Laboratory of Gansu Advanced Nonferrous Metal Materials under Grant SKL1311, the Key Laboratory of Eco-Environment-Related Polymer Materials of the Ministry of Education Program under Grant KF-13-01, and the Hongliu Young Teacher Cultivate Project of Lanzhou University of Technology under Grant Q201112.

REFERENCES

(1) Zhai, Y.; Dou, Y.; Zhao, D.; Fulvio, P. F.; Mayes, R. T.; Dai, S. *Adv. Mater.* **2011**, *23*, 4828−4850.
(2) Chmiola, J.; Yushin, G.; Gogotsi, Y.; Portet, C.; Simon, P.; Taberna, P. L. *Science* **2006**, *313*, 1760−1763.
(3) Xiong, W.; Liu, M.; Gan, L.; Lv, Y.; Li, Y.; Yang, L.; Xu, Z.; Hao, Z.; Liu, H.; Chen, L. *J. Power Sources* **2011**, *196*, 10461−10464.
(4) Yanwu, Z.; Shanthi, M.; Meryl, D. S.; Ganesh, K. J.; Cai, W.; Ferreira, P. J.; Adam, P.; Wallace, R. M.; Cychosz, K. A.; Matthias, T.; Dong, S.; Stach, E. A.; Ruoff, R. S. *Science* **2011**, *332*, 1537−1541.
(5) Jiang, H. L.; Liu, B.; Lan, Y. Q.; Kuratani, K.; Akita, T.; Shioyama, H.; Zong, F.; Xu, Q. *J. Am. Chem. Soc.* **2011**, *133*, 11854−11857.
(6) Lei, Z.; Bai, D.; Zhao, X. S. *Microporous Mesoporous Mater.* **2012**, *147*, 86−93.
(7) Shen, W.; Fan, W. *J. Mater. Chem. A* **2013**, *1*, 999−1013.
(8) Dhawale, D. S.; Benzigar, M. R.; Wahab, M. A.; Anand, C.; Varghese, S.; Balasubramanian, V. V.; Aldeyab, S. S.; Ariga, K.; Vinu, A. *Electrochim. Acta* **2012**, *77*, 256−261.
(9) Zhang, Y.; Li, G. Y.; Lv, Y.; Wang, L. Z.; Zhang, A. Q.; Song, Y. H.; Huang, B. *Int. J. Hydrogen Energy* **2011**, *36*, 11760−11766.
(10) Subramanian, V. *Solid State Ionics* **2004**, *175*, 511−515.
(11) Snook, G. A.; Kao, P.; Best, A. S. *J. Power Sources* **2011**, *196*, 1−12.
(12) Malak-Polaczyk, A.; Matei-Ghimbeu, C.; Vix-Guterl, C.; Frackowiak, E. *J. Solid State Chem.* **2010**, *183*, 969−974.
(13) Zhang, L. L.; Wei, T.; Wang, W.; Zhao, X. S. *Microporous Mesoporous Mater.* **2009**, *123*, 260−267.
(14) Zhang, K.; Zhang, L. L.; Zhao, X. S.; Wu, J. *Chem. Mater.* **2010**, *22*, 1392−1401.
(15) Li, L.; Song, H.; Zhang, Q.; Yao, J.; Chen, X. *J. Power Sources* **2009**, *187*, 268−274.
(16) Chem, J. M.; Ma, F.; Zhao, H.; Sun, L.; Li, Q.; Huo, L.; Xia, T.; Gao, S.; Pang, G. *J. Mater. Chem.* **2012**, *22*, 13464−13468.
(17) Zhang, D.; Hao, Y.; Zheng, L.; Ma, Y.; Feng, H.; Luo, H. *J. Mater. Chem. A* **2013**, *1*, 7584−7591.
(18) Tian, G. L.; Zhao, M. Q.; Zhang, Q.; Huang, J. Q.; Wei, F. *Carbon* **2012**, *50*, 5323−5330.
(19) Kim, N. D.; Kim, W.; Joo, J. B.; Oh, S.; Kim, P.; Kim, Y.; Yi, J. *J. Power Sources* **2008**, *180*, 671−675.
(20) Zhang, D.; Hao, Y.; Ma, Y.; Feng, H. *Appl. Surf. Sci.* **2012**, *258*, 2510−2514.
(21) Jeong, H. M.; Lee, J. W.; Shin, W. H.; Choi, Y. J.; Shin, H. J.; Kang, J. K.; Choi, J. W. *Nano Lett.* **2011**, *11*, 2472−2477.
(22) Ma, F.; Zhao, H.; Sun, L.; Li, Q.; Huo, L.; Xia, T.; Gao, S.; Pang, G.; Shi, Z.; Feng, S. *J. Mater. Chem.* **2012**, *22*, 13464−13468.
(23) Zhao, X.; Zhang, Q.; Chen, C. M.; Zhang, B.; Reiche, S.; Wang, A.; Zhang, T.; Schlögl, R.; Su, D. S. *Nano Energy* **2012**, *1*, 624−630.
(24) Seredych, M.; Bandosz, T. J. *J. Mater. Chem. A* **2013**, *1*, 1717−11727.
(25) Hasegawa, G.; Aoki, M.; Kanamori, K.; Nakanishi, K.; Hanada, T.; Tadanaga, K. *J. Mater. Chem.* **2011**, *21*, 2060−2063.
(26) Singh, K.; Seredych, M.; Castellon, R. E.; Bandosz, T. J. *ChemElectroChem* **2013**, DOI: 10.1002/celc.201300056.
(27) Kleitz, F.; Choi, S. H.; Ryoo, R. *Chem. Commun.* **2003**, *39*, 2136−2137.
(28) Vinu, A.; Anandan, S.; Anand, C.; Srinivasu, P.; Ariga, K.; Mori, T. *Microporous Mesoporous Mater.* **2008**, *109*, 398−404.
(29) Dou, Y. Q.; Zhai, Y.; Zeng, F.; Liu, X. X.; Tu, B.; Zhao, D. *J. Colloid Interface Sci.* **2010**, *341*, 353−358.
(30) Wu, Z.; Yang, Y.; Gu, D.; Li, Q.; Feng, D.; Chen, Z.; Tu, B.; Webley, P. A.; Zhao, D. *Small* **2009**, *5*, 2738−2749.
(31) Lv, Y.; Zhang, F.; Dou, Y.; Zhai, Y.; Wang, J.; Liu, H.; Xia, Y.; Tu, B.; Zhao, D. *J. Mater. Chem.* **2012**, *22*, 93−99.
(32) Liu, L.; Wang, F. Y.; Shao, G. S.; Ma, T. Y.; Yuan, Z. Y. *Carbon* **2010**, *48*, 2660−2664.
(33) Li, L.; Song, H.; Chen, X. *Microporous Mesoporous Mater.* **2006**, *94*, 9−14.
(34) Lei, Z.; Xiao, Y.; Dang, L.; Lu, M.; Yo, W. *Microporous Mesoporous Mater.* **2006**, *96*, 127−134.
(35) Xia, Y.; Mokaya, R. *Adv. Mater.* **2004**, *16*, 1553−1558.
(36) Liu, R.; Wu, D.; Feng, X.; Müllen, K. *Angew. Chem., Int. Ed.* **2010**, *49*, 2565−2569.

(37) Xu, X.; Li, Y.; Gong, Y.; Zhang, P.; Li, H.; Wang, Y. *J. Am. Chem. Soc.* **2012**, *134*, 16987−16990.
(38) Yang, Z.; Yao, Z.; Li, G.; Fang, U.; Nie, H.; Liu, Z.; Zhou, X.; Chen, X.; Huang, S. *ACS Nano* **2012**, *6*, 205−211.
(39) Xia, Y.; Zhu, Y.; Tang, Y. *Carbon* **2012**, *50*, 5543−5553.
(40) Hong, J.; Xia, X.; Wang, Y.; Xu, R. *J. Mater. Chem.* **2012**, *22*, 15006−15012.
(41) Paraknowitsch, J. P.; Thomas, A.; Schmidt, J. *Chem. Commun.* **2011**, *47*, 8283−8285.
(42) Chun, K. Y.; Lee, H. S.; Lee, C. J. *Carbon* **2009**, *47*, 169−177.
(43) Mane, G. P.; Talapaneni, S. N.; Anand, C.; Varghese, S. *Adv. Funct. Mater.* **2012**, *22*, 3596−3604.
(44) Reddy, A. L. M.; Srivastava, A.; Gowda, S. R.; Gullapalli, H.; Dubey, M.; Ajayan, P. M. *ACS Nano* **2010**, *4*, 6337−6342.
(45) Paraknowitsch, J. P.; Wienert, B.; Zhang, Y.; Thomas, A. *Chem.—Eur. J.* **2012**, *18*, 15416−15423.
(46) Puziy, A. M.; Poddubnaya, O. I.; Socha, R. P.; Gurgul, J.; Wisniewski, M. *Carbon* **2008**, *46*, 2113−2123.
(47) Lee, B. J.; Yoon, S.; Oh, S. M. *Adv. Mater.* **2000**, *12*, 359−362.
(48) Zhang, K.; Zhang, L. L.; Zhao, X. S.; Wu, J. *Chem. Mater.* **2010**, *22*, 1392−1401.
(49) Bandosz, T. J.; Matos, J.; Seredych, M.; Islam, M. S. Z.; Alfano, R. *Appl. Catal., A* **2012**, 445−446.
(50) Lai, L.; Yang, H.; Wang, L.; Zhong, J.; Chou, H.; Chen, L.; Chen, W.; Shen, Z.; Ruoff, R. S.; Lin, J. *ACS Nano* **2012**, *6*, 5941−5951.
(51) Wan, Y.; Qian, X.; Jia, N.; Wang, Z.; Li, H. *Chem. Mater.* **2008**, *20*, 1012−1018.
(52) Xiong, W.; Liu, M.; Gan, L.; Lv, Y.; Li, Y.; Yang, L.; Xu, Z.; Hao, Z.; Liu, H.; Chen, L. *J. Power Sources* **2011**, *196*, 10461−10464.
(53) Hulicova, D.; Yamashita, J.; Soneda, Y.; Hatori, H.; Kodama, M. *Chem. Mater.* **2005**, *17*, 1241−1247.
(54) Gong, K.; Du, F.; Xia, Z.; Durstock, M.; Dai, L. *Science* **2009**, *323*, 760−764.
(55) Wu, Z.-S.; Ren, W.; Xu, L.; Li, F.; Cheng, H. M. *ACS Nano* **2011**, *5*, 5463−5471.
(56) Ismagilov, Z. R.; Shalagina, A. E.; Yu, O.; Ischenko, A. V.; Kibis, L. S.; Boronin, A. I.; Chesalov, Y. A.; Kochubey, D. I.; Romanenko, A. I.; Anikeeva, O. B.; Buryakov, T. I.; Tkachev, E. N. *Carbon* **2009**, *47*, 1922−1929.
(57) Wiggins-Camacho, J. D.; Stevenson, K. J. *J. Phys. Chem. C* **2009**, *113*, 19082−19090.